Highly Dual-Heteroatom-Doped Ultrathin Carbon Nanosheets with Expanded Interlayer Distance for Efficient Energy Storage

Feili Lai,[†,‡,§] Gangyong Zhou,[†] Fei Li,[†] Zhihai He,[§] Dingyu Yong,[§] Wei Bai,[§] Yunpeng Huang,[‡] Weng Weei Tjiu,[∥] Yue-E Miao,*[†] Bicai Pan,[§] and Tianxi Liu*[†,‡]

[†]State Key Laboratory for Modification of Chemical Fibers and Polymer Materials, College of Materials Science and Engineering, Donghua University, Shanghai 201620, P. R. China

[‡]State Key Laboratory of Molecular Engineering of Polymers, Department of Macromolecular Science, Fudan University, Shanghai 200433, P. R. China

[§]Hefei National Laboratory for Physical Science at Microscale, Collaborative Innovation Center of Chemistry for Energy Materials, University of Science and Technology of China, Hefei, Anhui 230026, P. R. China

[∥]Institute of Materials Research and Engineering, A*STAR (Agency for Science, Technology and Research), 3 Research Link, Singapore 117602

S Supporting Information

ABSTRACT: Larger interlayer distance and higher doping efficiency of heteroatoms are considered to be the two most effective solutions to modulate the electronic structure of carbon materials to achieve improved electrochemical storage performances. Here, an innovative popping process is applied to puff biomaterials, i.e., the Chinese "five grains" of round-grained rice and wheat, into aerogels using the traditional Chinese popcorn machine. Thus, well-defined and interconnected three-dimensional pores are constructed within the biomaterial-derived carbon aerogels after a one-step pyrolysis process. As a result, the interlayer distance of the carbon nanosheets is slightly expanded from ∼3.6 to ∼3.7 Å, providing more expanded channels for rapid diffusion and adsorption of heteroatom precursors on the surface of the carbon layers. Therefore, a high amount of nitrogen and sulfur incorporation has been realized in the pyrolyzed carbon nanosheets, which further expand the interlayer distance between the carbon layers from ∼3.7 to ∼4.0 Å. These N, S dual-doped carbon nanosheets, derived from both rice and wheat, display outstanding energy storage performances, thus demonstrating the general ability or possibility of the traditional Chinese popping strategy to convert other biomaterials into similar carbon nanosheets with expanded interlayer distance and enhanced heteroatom doping efficiency.

KEYWORDS: Biomaterial, Ultrathin carbon nanosheet, Dual-heteroatom doping, Supercapacitor, Lithium-ion battery
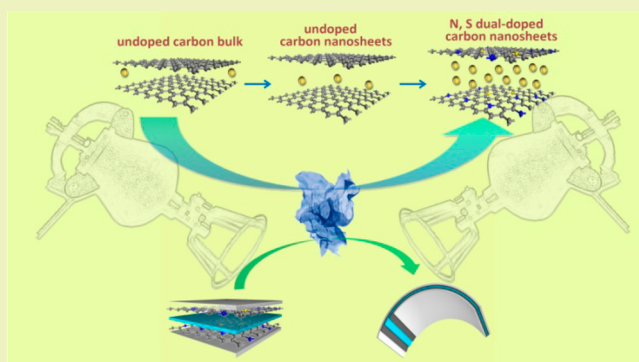
INTRODUCTION

Overexcessive consumption and gradual depletion of non-renewable energy resources have fuelled the development of clean and renewable modern energy systems.[1−5] Therefore, affordable energy storage devices with high power/energy densities, such as supercapacitors and lithium-ion batteries (LIBs), are regarded as one of the most promising alternatives for effective and temporary storage of excess electric energy.[6−12] Conventionally, commercialized graphite is the most widely used electrode material for supercapacitors and LIBs due to its good processability and low cost. However, the poorly developed pore texture of graphite dramatically hinders the diffusion of electrolyte ions into its inner space during the electrochemical reaction processes.[13] To maximally exert the energy storage properties, the development of advanced carbon materials, such as graphene, carbon nanotubes, and biomass-derived carbons, has been a key issue to achieve high specific surface area for increased ion adsorption.[14−16] As a typical atomic-scale carbon allotrope with two-dimensional (2D) structure and high specific surface area, graphene possesses high in-plane electrical conductivity which provides efficient channels for electron transport.[17,18] Yang et al. reported the capillary compression of adaptive graphene gel films in the presence of a nonvolatile liquid electrolyte to form a continuous ion transport network in the graphene film for the electrochemical reaction process.[19] Nevertheless, until now, graphene is mainly prepared by the Hummers method, ultrasound exfoliation, or chemical vapor deposition,[20−23]
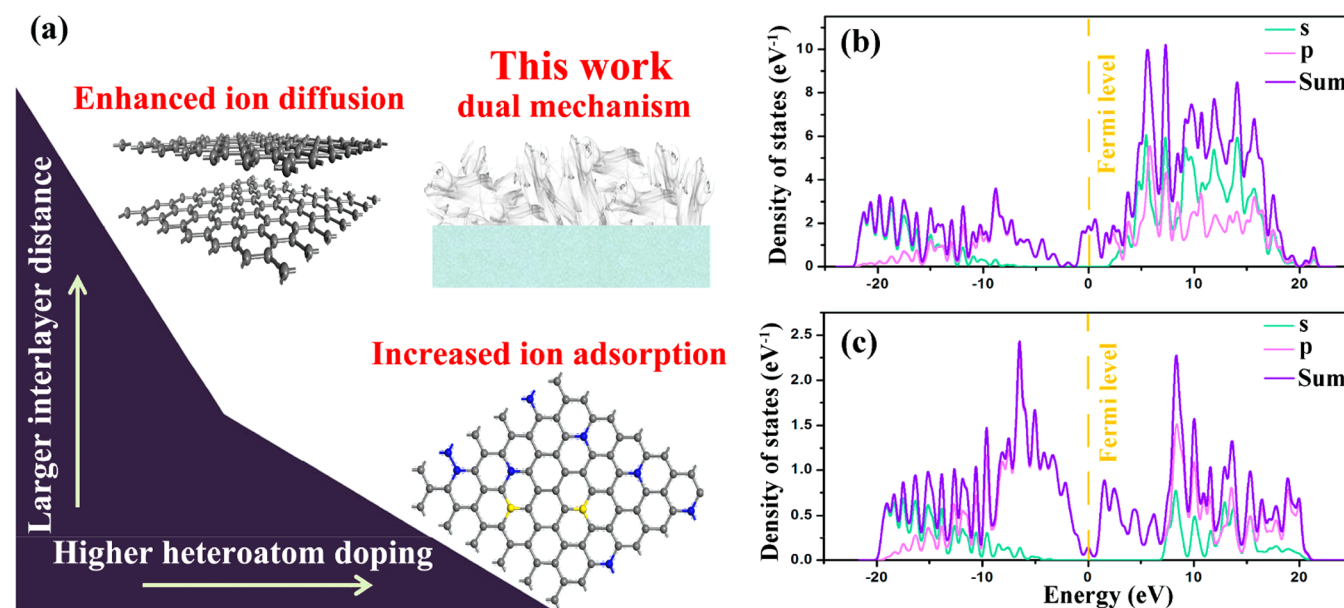
Figure 1. (a) Proposed dual mechanism to improve the energy storage properties of carbon-based materials. Calculated density of states for (b) N and S dual-doped carbon and (c) undoped carbon.
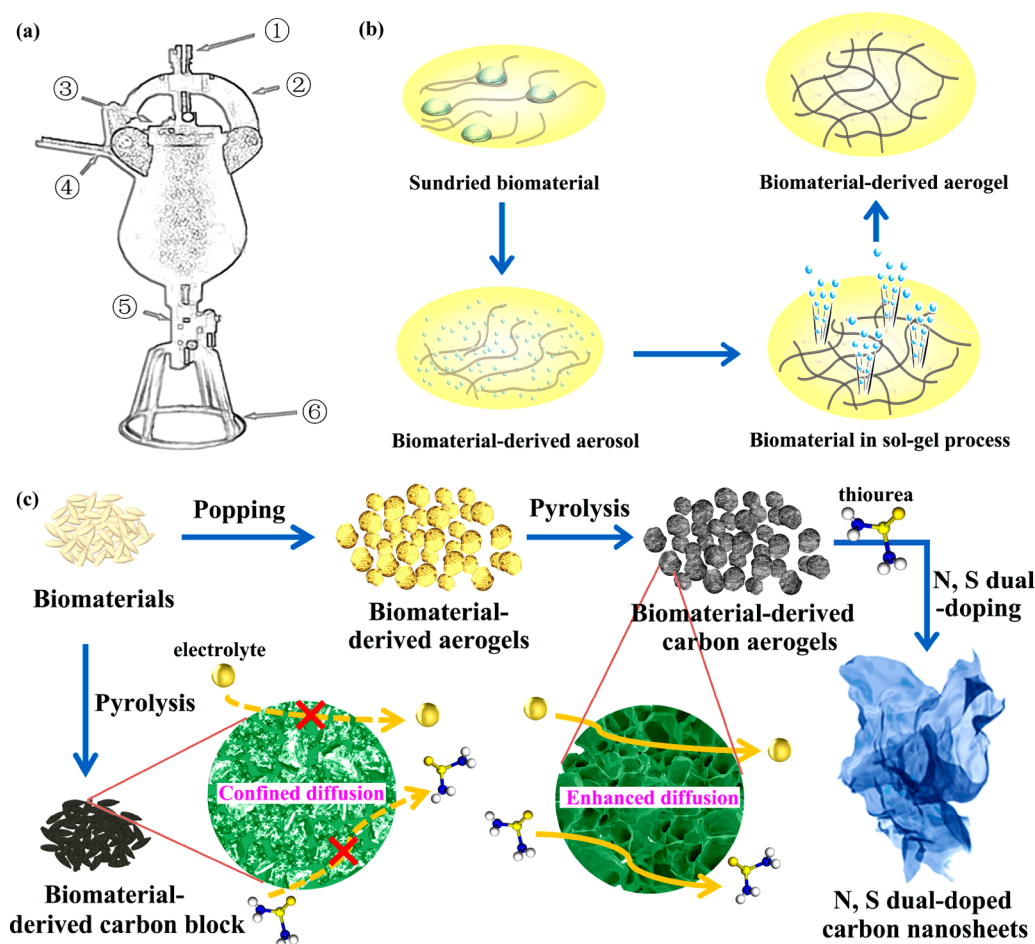

Figure 2. (a) Structure diagram of the traditional Chinese popcorn machine, where 1−6 represent the head screw, long radius elbow, machine cover, eyesight elbow, cotter, and handle, respectively. (b) Schematic illustration for the sol−gel transformation in the biomaterials during the popping process. (c) Schematic illustration for the preparation of biomaterial-derived N, S dual-doped carbon nanosheets with detailed diffusion process of thiourea and electrolyte in the biomaterial-derived carbon block and carbon aerogels.
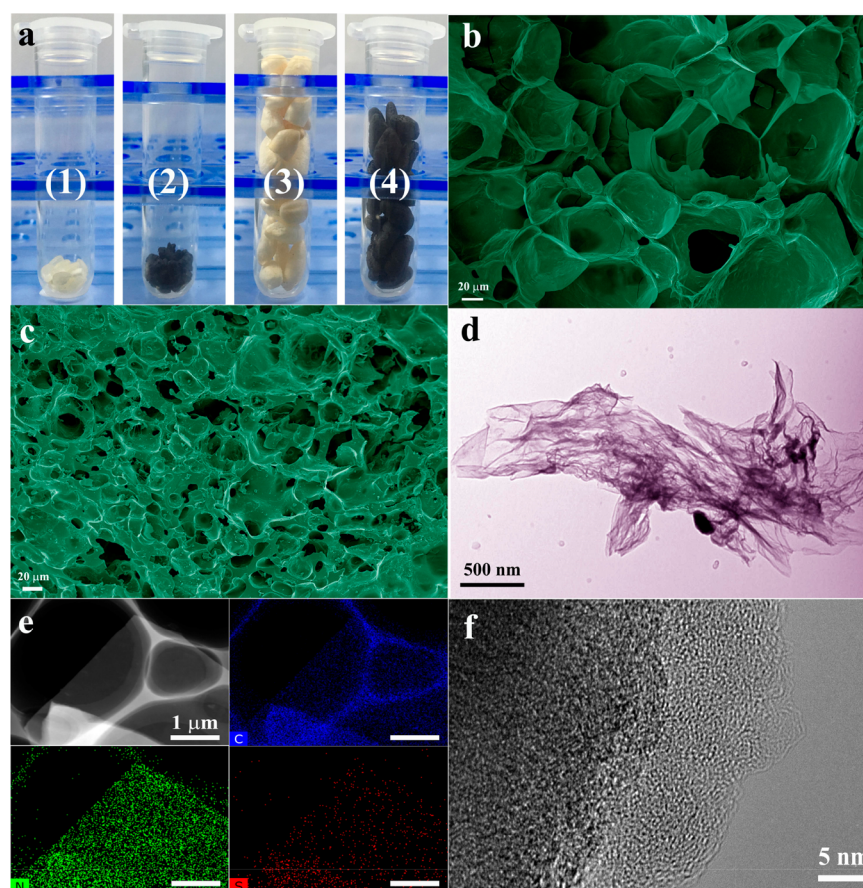
Figure 3. (a) Digital photographs of polished round-grained rice, RCB, round-grained rice aerogel (RA), and RCA. SEM images of (b) RCA and (c) RCB. (d) TEM image of N,S-RCSs. (e) TEM image of N,S-RCSs with the corresponding elemental mapping images of C, N, and S. (f) HR-TEM image of N,S-RCSs.

which generally involve high-cost and low-efficiency processes. Therefore, the ongoing search for alternative carbon-based materials with both excellent electrochemical performance and economic benefits has become one of the most intensive research areas.

Biomaterials, e.g., cellulose, willow catkin, bagasse, and coconut shells,[13,24−28] have been considered as the promising precursors to fabricate carbon-based energy storage electrodes due to their abundance, green chemical processes, and renewability. The "five grains" are a typical set of biomass materials from ancient China consisting of five kinds of farm crops, i.e., polished round-grained rice, wheat, red bean, soybean, and yellow millet. However, the untreated farm crops are only able to produce solid carbon structures with low specific surface area which can only store a limited amount of electric charge as electrode materials.[29] To enhance the ion penetration into the interlayers as well as to increase the ion adsorption on the surface of the carbon matrix, we propose two feasible solutions here, i.e., larger interlayer distance and higher heteroatom doping efficiency (as illustrated in Figure 1a). On one hand, an increased interlayer distance of the conventional graphite (∼0.335 nm) can largely facilitate the ion diffusion and storage in the inner space of the carbon material. On the other hand, substitutional heteroatom doping into the carbon matrix enables effective tailoring of its electron-donor properties and manipulation of its surface chemistry. Among the various possible dopants such as boron (B),[30] fluorine (F),[31] nitrogen (N),[32] phosphorus (P),[33] and sulfur (S),[34] the two proven

more facile methods to modulate the carbon structure as well as to maintain its high electrical conductivity are realized via N doping and S doping.[35−37] The density-functional-theory (DFT) calculations in Figure 1b,c reveal that nitrogen, sulfur dual-doped carbon possesses a raised Fermi level and increased density of states (DOS) around the Fermi level as compared to the undoped carbon, which can greatly improve its electronic conductivity to obtain high-performance energy storage materials.

Inspired by the daily popcorn making using the traditional Chinese popcorn machine (Figure 2a), we find that the traditional Chinese popping technique can be a facile strategy to incorporate porous structures into biomaterial-derived materials. From the molecular perspective, the popping process involves a sol−gel transformation as shown in Figure 2b. First, a certain amount of free water and bound water contained in the inner space of the sun-dried biomaterial easily evaporates to form the starch-based aerosol. Subsequently, the instantaneous heat-driven cross-linking effect leads to the rapid transition from biomaterial-derived aerosol into aerogel, accompanied by the outrush of steam and inburst of cold air. Thus, abundant pores are essentially incorporated into the inner space of the biomaterial-derived aerogel to form a three-dimensional porous structure. Herein, biomaterial-derived carbon aerogels are obtained first with well-defined and interconnected three-dimensional porous structures by using the traditional Chinese popcorn machine combined with a one-step pyrolysis process (Figure 2c). This allows the heteroatom precursor of thiourea
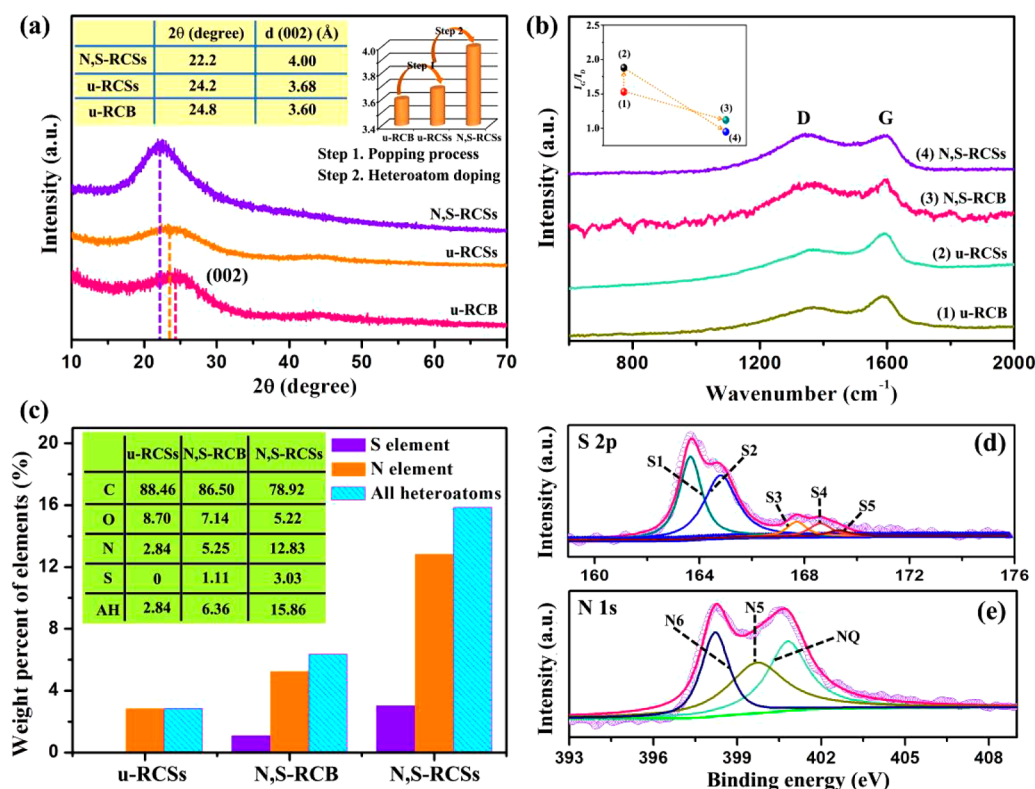
Figure 4. (a) XRD patterns of u-RCB, u-RCSs, and N,S-RCSs (inset: 2θ values and the corresponding interlayer distances of the (002) planes). (b) Raman spectra of different samples (inset: the variation of I_G/I_D values before and after the heteroatom doping of u-RCB and u-RCS samples). (c) Calculated weight percentages of C, O, N, and S elements for u-RCSs, N,S-RCB, and N,S-RCSs by XPS analysis (AH stands for all heteroatoms). High-resolution XPS spectra of (d) S 2p and (e) N 1s of N,S-RCSs.

molecules to diffuse and adsorb on the surface of biomaterial-derived carbon aerogels more easily than that of the corresponding carbon block, which leads to a dramatic increase of nitrogen and sulfur dual-doping amounts from ∼3% to ∼18%. As anticipated, the symmetric supercapacitor assembled by these rice-derived N, S dual-doped carbon nanosheets exhibits a high energy density of 20.6 W h kg^{-1} at a power density of 225 W kg^{-1}. Similarly, the wheat-derived N, S dual-doped carbon nanosheets are applied as anodes, which simultaneously show a discharge specific capacity of 1057 mA h g^{-1} at the first cycle and good rate/cycling stability toward lithium-ion battery applications.

■ RESULTS AND DISCUSSION

As aforementioned in Figure 1a, larger interlayer distance and higher efficiency of heteroatom doping are the two key solutions to enhance the electrochemical properties of carbon-based materials. However, the solid structure of the "five grains" (taking polished round-grained rice and wheat as two examples) makes it very difficult for the diffusion of both thiourea and electrolyte into the inner space. To overcome the intrinsic defect of these biomaterials, the popping mechanism is applied to obtain biomaterial-derived aerogels by using Chinese popcorn machine. This popping process (Figure S1) can facilely introduce puffed structures into the biomaterials, which is able to not only decrease the thickness of the pore walls but also increase the effective adsorption sites for thiourea molecules.

Polished round-grained rice is taken as the first example. As shown in Figure 3a, the volume of the pristine polished round-grained rice is being expanded several times into round-grained

rice aerogel after the popping process. After subsequent heat treatment under inert atmosphere, the round-grained rice aerogel is pyrolyzed into the corresponding carbon aerogel with only a slight volume shrinkage. Figure 3b,c shows the scanning electron microscope (SEM) images of the microstructure of the carbon aerogel and carbon block, respectively. It can be seen that the rice-derived carbon aerogel (RCA) is constructed of thin carbon walls which form a well-defined and interconnected three-dimensional (3D) porous structure with the pore size ranging from several tens to hundreds of micrometers. In contrast, the rice-derived carbon bulk (RCB) still maintains a solid surface with shallow holes, which will hinder the diffusion of thiourea molecules into the inner space for a uniform and efficient heteroatom-doping process. From the Brunauer−Emmett−Teller (BET) analysis (Figure S2a), the calculated specific surface area of RCA (111.5 m^2 g^{-1}) is about 33 times higher than that of RCB (3.3 m^2 g^{-1}). This shows that porous structures can be efficiently produced via the popping process under high pressure. The pore size distribution of RCA ranges from 2 to 50 nm (Figure S2b), favoring the efficient diffusion and adsorption of the thiourea molecules into the inner space of the carbon skeleton as well as on the surface of the carbon walls. Therefore, rice-derived N, S dual-doped carbon nano-sheets (N,S-RCSs) are obtained by using RCA as an ideal carbon source. As shown in the transmission electron microscope (TEM) image (Figure 3d), N,S-RCSs display a much thinner nanosheet structure as compared to that of the rice-derived N, S dual-doped carbon bulk (N,S-RCB, Figure S3) obtained without the popping treatment. In addition, the corresponding elemental mapping images (Figure 3e) indicate that the nitrogen and the sulfur atoms have been successfully
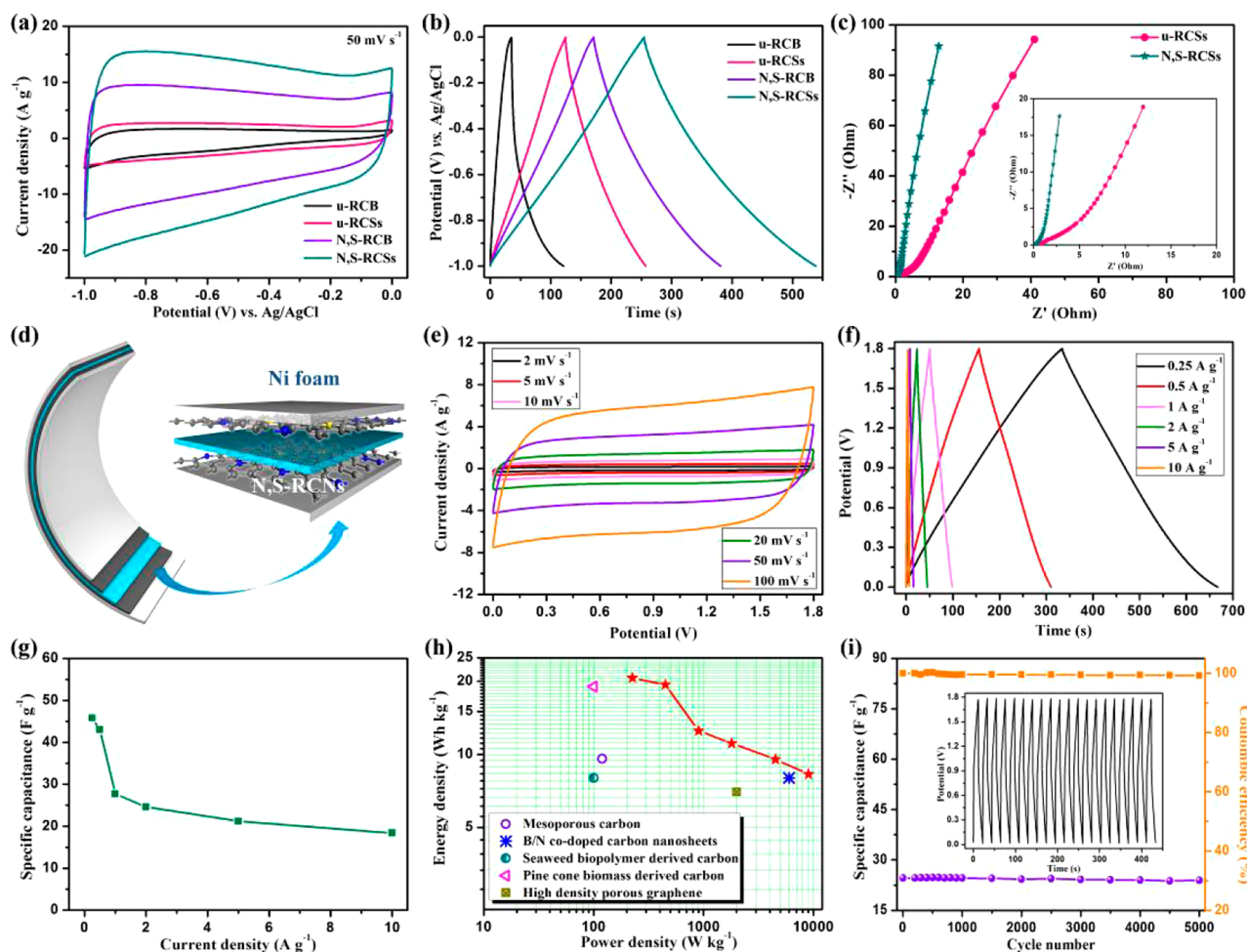
Figure 5. (a) CV curves at a scan rate of 50 mV s^{-1}, and (b) galvanostatic charge–discharge curves at 1 A g^{-1} for u-RCB, u-RCSs, N,S-RCB, and N,S-RCS electrodes in a three-electrode system. (c) Nyquist plots of u-RCSs and N,S-RCS electrodes. (d) Capacitive performance of the symmetric supercapacitor (N,S-RCSs//N,S-RCSs) with N,S-RCSs as both positive and negative electrode materials in 1.0 M Na$_2$SO$_4$ aqueous electrolyte. (e) CV curves of the as-assembled device at various scan rates. (f) Galvanostatic charge–discharge curves and (g) specific capacitances of the as-assembled device at various current densities. (h) Ragone plots of the as-assembled N,S-RCSs//N,S-RCSs device. (i) Cycling performance and the Coulombic efficiency of the symmetric supercapacitor at a current density of 2 A g^{-1} (inset: the charge–discharge curves of the last 20 cycles).

incorporated and homogeneously distributed throughout the carbon nanosheets. Highly disordered structure of N,S-RCSs is observed in the HR-TEM image (Figure 3f), demonstrating its poor crystal structure.

X-ray diffraction (XRD) data suggest the disordered structures of the carbon materials. As shown in Figure 4a, the diffraction peaks at 2θ of around 23° are assigned to the (002) planes of rice-derived undoped carbon bulk (u-RCB), rice-derived undoped carbon nanosheets (u-RCSs), and N,S-RCSs. It is worthwhile to note that a successive decline of the 2θ is observed for u-RCB (2θ = 24.8°), u-RCSs (2θ = 24.2°), and N,S-RCSs (2θ = 22.2°), with the corresponding interlayer distance calculated to be 3.60, 3.68, and 4.00 Å, respectively. Increments of the interlayer distances can be explained as follows: (1) The high pressure during the popping process facilitates the diffusion of moisture/oil molecules into the interlayer space, leading to the expansion of the interlayer distance from 3.60 to 3.68 Å. (2) The expanded interlayer distance favors the adsorption of thiourea molecules on the surface of carbon nanosheets, leading to a higher amount of heteroatom doping. Subsequent incorporation of heteroatoms further results in the expansion of the interlayer distance to 4.00

Å due to the larger atomic radius of nitrogen and sulfur atoms than that of carbon atom. Raman analyses are presented in Figure 4b, where the D band at ~1350 cm^{-1} and G band at ~1590 cm^{-1} represent the disordered degree and graphitic order of carbon materials, respectively.[38] The higher I_G/I_D value (determined by the specific values of their peak intensities) of u-RCSs (1.88) than that of u-RCB (1.53) demonstrates that the popping process is able to enhance the graphitic order of carbon materials. However, the disordered structures, attributed to the generated defects during the heteroatom-doping process, result in the decrease of I_G/I_D values of both N,S-RCB (I_G/I_D = 1.12) and N,S-RCSs (I_G/I_D = 0.95). Furthermore, a much sharper decrease in $\Delta I_G/I_D$ of N,S-RCSs ($\Delta I_G/I_D$ = 0.93) than that of N,S-RCB ($\Delta I_G/I_D$ = 0.41) indicates that the puffed RCA is able to facilitate the heteroatom-doping process and hence introduce more disordered structures into the 3D carbon skeletons.

The contents of N and S heteroatoms in various carbon samples are further determined by X-ray photoelectron spectroscopy (XPS) (Figure 4c). Only a low amount of nitrogen atoms in u-RCSs (Figure S5) is present, which originates from either the self-contained protein/amino acid or
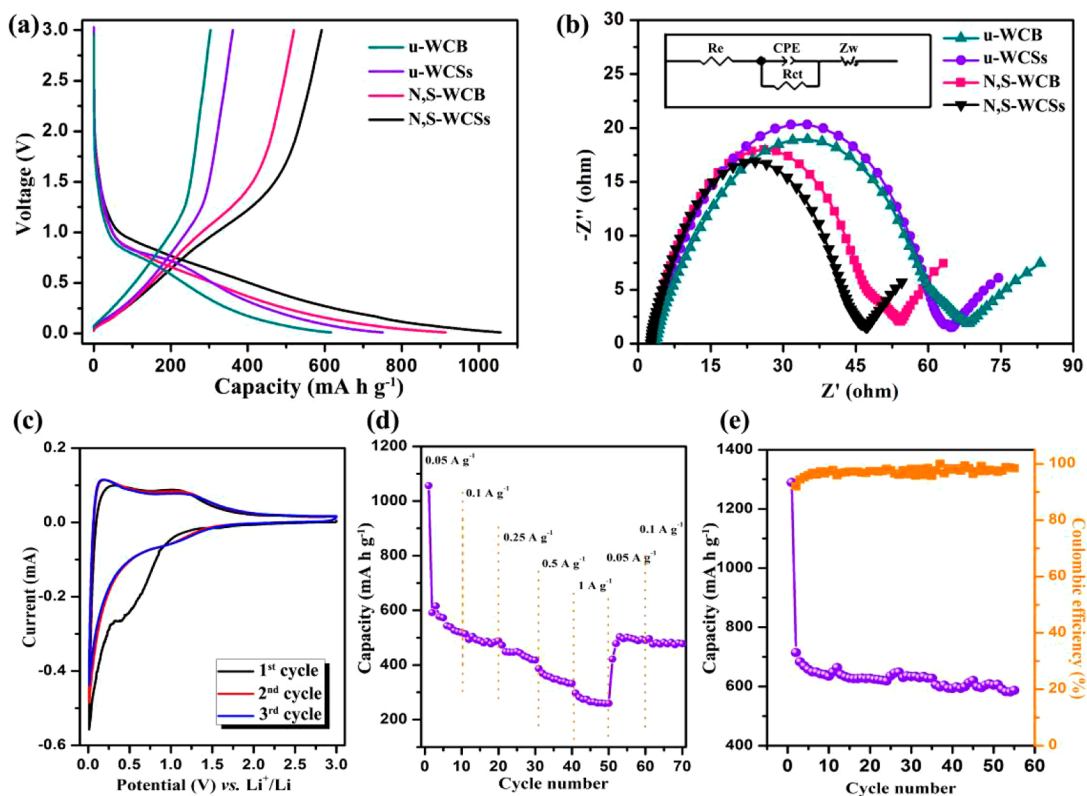
Figure 6. (a) Initial charge−discharge curves of u-WCB, u-WCSs, N,S-WCB, and N,S-WCS electrodes at a current density of 0.05 A g^{-1}. (b) Nyquist plots of u-WCB, u-WCSs, N,S-WCB, and N,S-WCS electrodes in the frequency range 10^5−10^{-2} Hz with an ac voltage amplitude of 5 mV. (c) First three CV cycles of the N,S-WCS electrode at a scan rate of 0.1 mV s^{-1} from 0.01 to 3 V. (d) Rate behavior of the N,S-WCS electrode at various current densities. (e) Cycling stability of the N,S-WCS electrode at a current density of 0.05 A g^{-1}.

the adsorbed nitrogen during the carbonization process.[39,40] The addition of thiourea as the precursor for heteroatom doping results in the introduction of nitrogen and sulfur atoms into the carbon structures for both N,S-RCB and N,S-RCSs with all-heteroatom weight percentages of 6.31% (1.11% for S atom, 5.25% for N atom) and 15.86% (3.03% for S atom, 12.83% for N atom), respectively. As anticipated, N,S-RCSs display a higher content of heteroatom than N,S-RCB. The detailed surface elemental composition and valence state of N,S-RCSs are identified with four distinct peaks for C, O, N, and S elements (Figure S6). In the S 2p spectrum (Figure 4d), two prominent peaks at 163.6 and 164.8 eV are assigned to the S 2p$_{3/2}$ (S1) and S 2p$_{1/2}$ (S2), which corresponds to the −C−S−C− covalent bond of thiophene-type sulfur.[41] Three minor peaks at higher binding energies of 167.7, 168.7, and 169.3 eV, respectively, are consistent with different oxidized sulfur forms of S3, S4, and S5 in the −C−SO$_x$−C− (where x = 2−4) sulfone bridges.[34,42] Meanwhile, the high-resolution N 1s spectrum (Figure 4e) is well-fitted into three peaks centered at 398.2, 399.7, and 400.8 eV, assigned to the pyridinic-like (N6), pyrrolic-like (N5), and graphitic (NQ) nitrogen, respectively. The structural defects thus generated by heteroatom doping in the carbon atomic layers will greatly increase the electron donor property as well as the charge mobility of N,S-RCSs for enhanced energy storage properties.

A three-electrode system was fabricated by using the rice-derived carbon materials as the supercapacitor working electrodes, Ag/AgCl as the reference electrode, and 6 M KOH as the aqueous electrolyte. Figure 5a shows the CV curves of various carbon-based electrodes (i.e., u-RCB, u-RCSs,

N,S-RCB and N,S-RCSs) in the potential range from −1.0 to 0 V at a scan rate of 50 mV s^{-1}. Near-rectangular shapes of the CV curves as well as the symmetrical and linear galvanostatic charge−discharge curves at a current density of 1 A g^{-1} (Figure 5b) indicate the double-layer capacitance characteristic of all these electrodes which originates from the ion diffusion/adsorption electrochemical processes. In particular, because of the expanded interlayer distance and higher heteroatom-doping amount, better capacitive performances are obtained for N,S-RCSs than for u-RCSs, u-RCB, and N,S-RCSs. Furthermore, with enhanced electronic conductivity and ion diffusion after the efficient doping of nitrogen and sulfur atoms, the N,S-RCS electrode shows reduced resistance compared to the u-RCS electrode (Figure 5c). Therefore, the N,S-RCS electrode displays an outstanding capacitance of 321 F g^{-1} at the current density of 0.5 A g^{-1} (Figure S7), which is also much more superior than other carbon-based materials being reported (Table S1 in the Supporting Information), such as polyaniline-coated bacterial cellulose (296 F g^{-1} at 2 mV s^{-1}),[43] tobacco-rod-derived carbon (287 F g^{-1} at 0.5 A g^{-1}),[41] and bagasse-derived carbon (137 F g^{-1} at 2 mV s^{-1}).[25]

For practical applications with wide working voltage windows, a symmetric supercapacitor device is assembled by using two N,S-RCS electrodes as shown in Figure 5d, which is marked as N,S-RCSs//N,S-RCSs device. Figure 5e shows that the potential window of the symmetric supercapacitor is largely extended to 0−1.8 V. The galvanostatic charge−discharge curves under different current densities (Figure 5f) show highly linear correlations and symmetrical shapes with a rapid $I−V$ response. Furthermore, the calculated specific capacitance
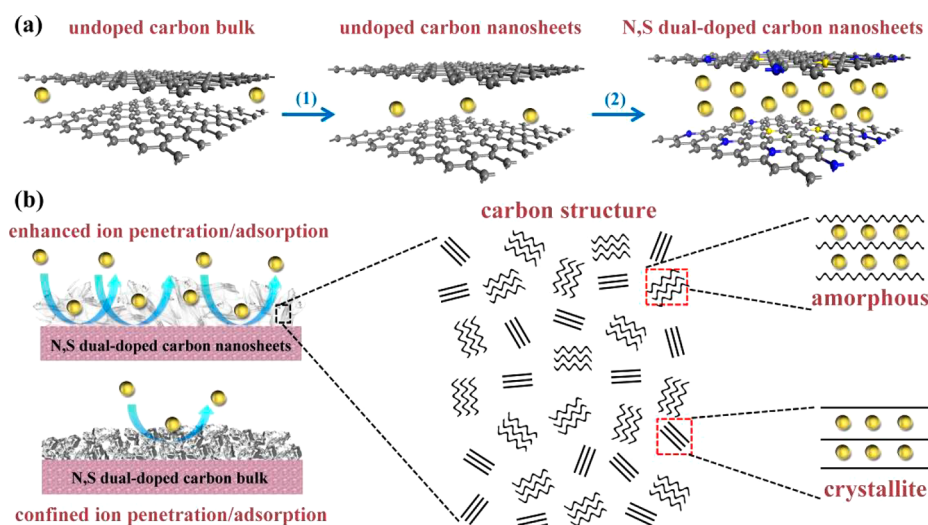
Figure 7. (a) Graphical illustration of the biomaterial-derived carbon bulk, biomaterial-derived undoped carbon nanosheets, and biomaterial-derived N, S dual-doped carbon nanosheets with different interlayer distances of ~3.6, ~3.7, and ~4.0 Å, respectively. The glittery yellow ball represents OH^-/Li^+ ions; the blue and yellow balls in the N, S dual-doped carbon nanosheets represent nitrogen and sulfur atoms, respectively. Steps 1 and 2 represent the popping and heteroatom-doping processes, respectively. (b) Schematic illustration showing the different energy storage mechanisms in biomaterial-derived N, S dual-doped carbon nanosheets and N, S dual-doped carbon bulk.

based on the total mass reaches 45.8 F g^{-1} at 0.25 A g^{-1} (Figure 5g). The Ragone diagram (Figure 5h) exhibits a high energy density of 20.6 W h kg^{-1} at the power density of 225 W kg^{-1}. This performance is superior to previously reported carbon-based symmetric supercapacitor devices, such as mesoporous carbon (9.6 W h kg^{-1} at 119.4 W kg^{-1}),[44] B/N codoped carbon nanosheets (8 W h kg^{-1} at 6000 W kg^{-1}),[45] seaweed biopolymer-derived carbon (8 W h kg^{-1} at 100 W kg^{-1}),[46] pine cone biomass-derived carbon (19 W h kg^{-1} at 100 W kg^{-1}),[47] and high-density porous graphene (7 W h kg^{-1} at 2000 W kg^{-1}).[48] For an investigation of the cycling stability of the as-assembled asymmetric supercapacitor device, a galvanostatic charge−discharge test was performed at a constant current density of 2 A g^{-1} for 5000 cycles. As shown in Figure 5i, 97.2% of the initial specific capacitance is still retained. More importantly, the Coulombic efficiency of the device remains 99.2% after the cycling tests as shown in the last 20 charge−discharge cycles (see inset of Figure 5i). Therefore, this work provides a combined method by employing the popping and heteroatom-doping processes to successfully modify biomass-derived carbon materials with significant improvement in energy storage performances.

For a demonstration of the universality of this method, another kind of Chinese "five grain", wheat, has been applied. As displayed in Figure S8a−c, the wheat-derived carbon aerogel (WCA) exhibits a well-interconnected 3D porous structure with numerous thin carbon walls which favors faster diffusion of thiourea molecules into the carbon skeleton. In contrast, the wheat-derived carbon bulk (WCB) shows a solid structure with closed channels for further heteroatom doping (Figure S9). As determined by BET analysis (Figure S11), the calculated specific surface area of WCA (79.1 m^2 g^{-1}) is more than 10 times higher than that of WCB (7.5 m^2 g^{-1}) . This further indicates that the popping process can efficiently puff the biomaterials and incorporate microporous structures in the corresponding aerogels. XRD patterns in Figure S13a demonstrate the two-step expansion of the interlayer distances, which are 3.63, 3.71, and 4.01 Å for wheat-derived undoped carbon bulk (u-WCB), wheat-derived undoped carbon nano-

sheets (u-WCSs), and wheat-derived N, S dual-doped carbon nanosheets (N,S-WCSs), respectively. The XPS results (Figures S13−S15) give evidence on the successful and enhanced doping of N and S atoms in the carbon matrix for N,S-WCSs. These wheat-derived carbon materials are then applied as electrode materials for lithium-ion batteries. Figure 6a shows typical first-cycle discharge/charge voltage curves of u-WCB, WCSs, N,S-WCB, and N,S-WCS electrodes, respectively. The voltage plateau at around 0.7 V is ascribed to the formation of the solid electrolyte interface (SEI) layers and electrolyte decomposition.[10,49] The discharge specific capacities of 618, 754, 913, and 1057 mA h g^{-1} and the charge specific capacities of 302, 360, 520, and 593 mA h g^{-1} are obtained for u-WCB, WCSs, N,S-WCB, and N,S-WCS electrodes, respectively. Because of the irreversible losses of the first cycles, the corresponding Coulombic efficiencies are 48.1%, 48.7%, 56.0%, and 60%, respectively. Meanwhile, EIS measurements are investigated to understand the electrochemical impedance of the u-WCB, WCSs, N,S-WCB, and N,S-WCB electrodes. The electrochemical impedance spectra of the u-WCB, u-WCSs, N,S-WCB, and N,S-WCS electrodes are shown in Figure 6b. All spectra are composed of a semicircle in the high-frequency region and an inclined line in the low-frequency region. It is well-known that the semicircle is related to the charge transfer resistance (R_{ct}) between the electrode and electrolyte interface, while the sloping line in the low frequency is the Warburg impedance (Z_W), attributed to the Li$^+$ ion diffusion in the solid electrode.[50] The equivalent circuit is inserted into Figure 6b, where R_e stands for the resistance of the whole reaction system, including the electrolyte resistance, the physical resistances between the electrode and electrolyte interface, and the constant phase element (CPE) which is a double-layer capacitance on the electrode surface. Table S2 provides the R_e and R_{ct} fitting values of u-WCB, u-WCSs, N,S-WCB, and N,S-WCS electrodes, in view of the fact that R_{ct} is a major part of the internal resistance of a battery. It shows that the R_{ct} values are 61.49, 59.74, 47.73, and 43.07 Ω for u-WCB, WCSs, N,S-WCB, and N,S-WCS electrodes, respectively. Obviously, the N,S-WCS electrode has the lowest R_{ct} value, owing to the

expanded distance between the carbon interlayers and improved conductivity induced by the dual-doped nitrogen and sulfur atoms in carbons. To reveal its electrochemistry of the lithiation/delithiation process, the first, second, and third cycles of CV curves are collected for the N,S-WCS-based cell in the potential window 0.01−3.0 V at a scan rate of 0.1 mV s^{-1} (Figure 6c). Two peaks appear at 0.45 and 1.54 V during the first cycle, and disappear during the second and third cycles, which is assigned to the irreversible consumption of charge due to the generation of the SEI layer.[51] In the cathodic scanning, the peak near 0 V is ascribed to the Li-ion insertion into the N,S-WCS structures.[52] It is worthwhile to note that the CV curves of the subsequent cycles are well-overlapped, indicating an outstanding lithium storage reversibility. Furthermore, the rate capability of the N,S-WCS electrode is investigated by applying various current densities (Figure 6d). The N,S-WCS electrode delivers a high reversible capacity of ∼300 mA h g^{-1} under the high current density of 1 A g^{-1}, and restores to ∼500 mA h g^{-1} (approaching 90% of its initial charge capacity) when the current rate is being recharged to 0.05 A g^{-1}. Despite an irreversible capacity loss due to the formation of SEI layers and the trapped lithium in the carbon structure during the first cycle, the N,S-WCS electrode is still able to retain a high discharge capacity of 586.85 mA h g^{-1} at 0.05 A g^{-1} after 55 cycles (Figure 6e). The Coulombic efficiency is also maintained at almost 100% since the second cycle, demonstrating the excellent cycling performance of the N,S-WCS electrode with a reversible retention of 100%.

In view of the above results, we have demonstrated an efficient and general method to achieve dual heteroatom-doped ultrathin carbon nanosheets with expanded interlayer distance as well as high heteroatom doping efficiency by using the traditional Chinese popcorn machine and thiourea as the heteroatom precursor. As shown in Figure 7a, the popping process can effectively expand the carbon atomic interlayer distance from ∼3.6 to ∼3.7 Å, while the subsequent introduction of heteroatoms results in a further increase of the interlayer distance to ∼4.0 Å. Thus, the ion (including OH^{-} and Li^{+}) diffusion and adsorption on both the amorphous and crystalline structures of carbon nanosheets are remarkably facilitated (Figure 7b), leading to their high-performance energy storage properties.

■ CONCLUSIONS

In summary, we introduce a robust route to fabricate heteroatom-doped carbon nanosheets derived from biomaterials of Chinese "five grains" for supercapacitor and lithium-ion battery applications. The popping process via the traditional Chinese popcorn machine is first used to puff the biomaterials into the corresponding aerogels. Interconnected three-dimensional pores with expanded interlayer distance from ∼3.6 to ∼3.7 Å have been successfully achieved after a one-step pyrolysis. This results in much easier diffusion of the thiourea precursor into the inner space for high doping efficiency of heteroatoms, which leads to further increase in the interlayer distance of ∼4.0 Å. The two-step expansion of the interlayer distance and efficiently doped heteroatoms endow the biomaterial-derived carbon nanosheets with enhanced ion diffusion and adsorption in the carbon structures. Therefore, the symmetric supercapacitor assembled from rice-derived N, S dual-doped carbon nanosheets delivers a high specific capacitance of 45.8 F g^{-1} at the current density of 0.25 A g^{-1}, and an outstanding energy density of 20.6 W h kg^{-1} at the

power density of 225 W kg^{-1}. Meanwhile, the wheat-derived N, S dual-doped carbon nanosheets are used as anode for a lithium-ion battery, which shows a high specific capacity of 1057 mA h g^{-1} and good rate/cycling stability. The dramatically enhanced electrochemical performances imply that the general method put forward in this work by using popping and heteroatom-doping processes is efficient to change various biomaterials into high-quality carbon materials for high-performance energy storage applications.

■ EXPERIMENTAL SECTION

Materials. All chemicals used in this study are of analytical grade and were used as received. Thiourea was purchased from Sinopharm Chemical Reagent Co.

Synthesis of Biomaterial-Derived Aerogels and Carbon Aerogels. First, the polished round-grained rice was washed with deionized water and dried under the sun for several days to remove the excess moisture. Subsequently, the round-grained rice was poured into the traditional Chinese popcorn machine and uniformly heated until it popped into round-grained rice aerogel (RA). Then, the RA was heated up to 400 °C in N$_2$ atmosphere with a heating rate of 5 °C min^{-1} and maintained for 1 h to obtain round-grained rice-derived carbon aerogel (RCA). Meanwhile, the round-grained rice without popping treatment was subjected to similar pyrolysis processes to obtain round-grained rice-derived carbon block (RCB).

Similarly, wheat aerogel (WA), and wheat-derived carbon aerogel (WCA) and carbon block (WCB) were obtained via similar procedures.

Synthesis of N, S Dual-Doped and Undoped Carbon Materials. For the synthesis of N, S dual-doped carbon samples, the thiourea (CN$_2$H$_4$S) with both nitrogen and sulfur atoms was used as the precursor. RCA/WCA and the thiourea were ground together at a mass ratio of 1:4 to form the mixed powder. Then, the mixed powder was heated up to 850 °C in N$_2$ atmosphere with a heating rate of 5 °C min^{-1} and maintained for 3 h to obtain rice-/wheat-derived N, S dual-doped carbon nanosheets (N,S-RCSs/N,S-WCSs). After heat treatment, the sample was washed with water and ethanol, and dried at 60 °C overnight. For comparison purposes, RCB/WCB were also subjected to similar processes to obtain rice-/wheat-derived N, S dual-doped carbon bulk (N,S-RCB/N,S-WCB).

Meanwhile, rice-/wheat-derived undoped carbon nanosheets (u-RCSs/u-WCSs), and rice-/wheat-derived undoped carbon bulk (u-RCB/u-RWB) were also obtained by direct carbonization of RCA, WCA, RCB, and WCB without the addition of thiourea.

Characterization. Morphology of the samples was observed by field emission scanning electron microscope (FE-SEM) by using an FEI Sirion-200 SEM. Transmission electron microscopy (TEM), high-resolution TEM (HR-TEM), and elemental mapping images were acquired by using a JEOL-2010 TEM with an accelerating voltage of 200 kV. X-ray diffraction (XRD) patterns were obtained by a Philips X'Pert Pro Super diffractometer using Cu Kα radiation (λ = 1.5418 Å). X-ray photoelectron spectra (XPS) were acquired by an ESCALAB MK II instrument with Mg Kα as the excitation source. The binding energies obtained in the XPS spectral analysis were corrected for specimen charging by referencing C 1s to 284.8 eV. Raman spectra were detected by a Renishaw RM3000 Micro-Raman system. BET nitrogen adsorption−desorption was measured by using a Micromeritics ASAP 2000 system. Thermogravimetric analysis (Pyris 1 TGA, PerkinElmer) was performed in air from 20 to 800 °C at a heating rate of 20 °C min^{-1}.

First-Principles Calculations. The first-principles calculations were performed on the basis of the density functional theory (DFT) implemented in the VASP package.[53] The interaction between ions and valence electrons was described with projector augmented wave (PAW) potentials,[54−56] and the exchange-correlation between electrons was described using the generalized gradient approximation (GGA) in the Perdew−Burke−Ernzerhof (PBE) form.[57] The kinetic energy cutoff for the plane-wave basis set was 550 eV. A 6 × 6 × 1 graphite-like carbon supercell with a vacuum region of 15 Å was

adopted, and its Brillouin zone was sampled with $3 \times 3 \times 1$ k points within the γ-centered Monkhorst−Pack scheme.[58] In our calculations, the atomic coordinates were fully relaxed until the forces on all the atoms were less than 0.01 eV Å^{-1}.

Electrochemical Measurements for Supercapacitors. The supercapacitor electrodes were prepared according to the previously reported work.[59] Briefly, the working electrode was prepared by mixing the above samples, carbon black, and poly(tetrafluoroethylene) at a mass ratio of 8:1:1 to obtain a slurry. Subsequently, the slurry was pressed onto the nickel foam current collector at a fixed mass loading (3 mg cm^{-2}) of active material and dried at 80 °C for 12 h.

The electrochemical measurements were performed in 6 M KOH aqueous solution on an electrochemical working station (CHI660D, Chenhua Instruments Co. Ltd., Shanghai, China) with a standard three-electrode setup, where the Ag/AgCl and Pt wire were used as the reference and counter electrode, respectively. Cyclic voltammograms (CVs) were conducted between −1 and 0 V. Galvanostatic charge−discharge (GCD) test was performed from −1 to 0 V. The electrochemical impedance spectroscopy (EIS) measurements were conducted by applying an ac voltage in the frequency range from 10 mHz to 100 kHz with an amplitude of 5 mV.

The symmetric supercapacitor devices were constructed using two electrodes with the same loading amount of electroactive materials, which were then conducted in the voltage range 0−1.8 V.

The specific capacitance (C_s) can be calculated from the galvanostatic charge−discharge curves according to the following equation:

$$C_s = \frac{I \times \Delta t}{m \times v} \tag{1}$$

where I (A) is the current, Δt (s) is the discharge time, m (g) is the total mass of electroactive materials in both the three-electrode and two-electrode systems, and v (V) is the potential.

The energy density E (W h kg^{-1}) and power density P (W kg^{-1}) are calculated according to the following equations:

$$E = \frac{1}{2} \times C \times V^2 \tag{2}$$

$$P = \frac{E}{\Delta t} \tag{3}$$

where C (F g^{-1}) is the specific capacitance based on the total mass of electroactive materials, V (V) is the discharge potential range, and Δt (s) is the discharge time.

Electrochemical Measurements for Lithium-Ion Batteries. Coin-type half-battery cells were assembled in an argon-filled glovebox (M. Braun Inert Gas Systems Co. Ltd.) with the concentrations of moisture and oxygen below 0.1 ppm. Here, the polypropylene film (Celgard-2400) was employed as the separator, lithium foil was served as the counter and reference electrodes, and 1 M LiPF$_6$ solution in ethylene carbonate (EC)/dimethyl carbonate (DMC)/diethyl carbonate (DEC) (1:1:1, v/v/v) was applied as the electrolyte. The working anodes were prepared by a slurry-coating procedure on a pure copper foil. The slurry was prepared by uniformly dispersing the carbon-based samples, acetylene black, and poly(vinylidene fluoride) (8:1:1, w/w/w) in N-methyl-2-pyrrolidinone solution. Cyclic voltammetry (CV) curves were collected on a CHI660D electrochemical workstation (Chenhua Instruments Co. Ltd.) in the potential range 0.01−3.0 V at a scan rate of 0.1 mV s^{-1}. CT2013A cell test instrument (LAND Electronic Co. Ltd.) was used to carry out the galvanostatic discharge−charge measurements and rate-performance tests in the voltage range 0.01−3.0 V. The EIS was measured in the frequency range from 100 kHz to 0.01 Hz at the open circuit potential with an ac voltage amplitude of 5.0 mV.

■ ASSOCIATED CONTENT

ⓢ Supporting Information

The Supporting Information is available free of charge on the ACS Publications website at DOI: 10.1021/acssusche-meng.7b03161.

Digital photographs, nitrogen adsorption−desorption isotherms, TEM images, TGA profiles, XPS spectra, CV curves, galvanostatic charge−discharge curves, specific capacitances, cycling stabilities, SEM images, pore size distribution, Raman spectra, weight percentages, and comparisons of capacitive properties (PDF)

■ AUTHOR INFORMATION

Corresponding Authors
*E-mail: yuee_miao@dhu.edu.cn.
*E-mail: txliu@dhu.edu.cn.

ORCID ⃝

Yue-E Miao: 0000-0002-3660-029X
Bicai Pan: 0000-0002-5128-7860
Tianxi Liu: 0000-0002-5592-7386

Notes

The authors declare no competing financial interest.

■ ACKNOWLEDGMENTS

■ REFERENCES

(1) Arico, A. S.; Bruce, P.; Scrosati, B.; Tarascon, J. M.; Van Schalkwijk, W. Nanostructured materials for advanced energy conversion and storage devices. *Nat. Mater.* **2005**, *4*, 366−377.

(2) Qi, D. P.; Liu, Y.; Liu, Z. Y.; Zhang, L.; Chen, X. D. Design of architectures and materials in in-plane micro-supercapacitors: Current status and future challenges. *Adv. Mater.* **2017**, *29*, 1602802.

(3) Zheng, S. S.; Li, X. R.; Yan, B. Y.; Hu, Q.; Xu, Y. X.; Xiao, X.; Xue, H. G.; Peng, H. Transition-metal (Fe, Co Ni) based metal-organic frameworks for electrochemical energy storage. *Adv. Energy Mater.* **2017**, *7*, 1602733.

(4) Zhang, Y. Y.; Rui, X. H.; Tang, Y. X.; Liu, Y. Q.; Wei, J. Q.; Chen, S.; Leow, W. R.; Li, W. L.; Liu, Y. J.; Deng, J. Y.; Ma, B.; Yan, Q. Y.; Chen, X. D. Wet-chemical processing of phosphorus composite nanosheets for high-rate and high-capacity lithium-ion batteries. *Adv. Energy Mater.* **2016**, *6*, 1502409.

(5) Lu, Y.; Li, B.; Zheng, S. S.; Xu, Y. X.; Xue, H. G.; Pang, H. Syntheses and energy storage applications of M_xS_y (M = Cu, Ag, Au) and their composites: Rechargeable batteries and supercapacitors. *Adv. Funct. Mater.* **2017**, *27*, 1703949.

(6) Zhang, L. L.; Zhao, X. S. Carbon-based materials as super-capacitor electrodes. *Chem. Soc. Rev.* **2009**, *38*, 2520−2531.

(7) Wang, H. L.; Casalongue, H. S.; Liang, Y. Y.; Dai, H. J.Ni(OH)$_2$ nanoplates grown on graphene as advanced electrochemical pseudocapacitor materials. *J. Am. Chem. Soc.* **2010**, *132*, 7472−7477.

(8) Zhao, Y.; Liu, J.; Hu, Y.; Cheng, H. H.; Hu, C. G.; Jiang, C. C.; Jiang, L.; Cao, A. Y.; Qu, L. T. Highly compression-tolerant supercapacitor based on polypyrrole-mediated graphene foam electrodes. *Adv. Mater.* **2013**, *25*, 591−595.

(9) Bruce, P. G.; Scrosati, B.; Tarascon, J. M. Nanomaterials for rechargeable lithium batteries. *Angew. Chem., Int. Ed.* **2008**, *47*, 2930−2946.

(10) Miao, Y. E.; Huang, Y. P.; Zhang, L. S.; Fan, W.; Lai, F. L.; Liu, T. X. Electrospun porous carbon nanofiber@MoS2 core/sheath fiber membranes as highly flexible and binder-free anodes for lithium-ion batteries. *Nanoscale* **2015**, *7*, 11093−11101.

(11) Lv, Z. S.; Luo, Y. F.; Tang, Y. X.; Wei, J. Q.; Zhu, Z. Q.; Zhou, X. R.; Li, W. L.; Zeng, Y.; Zhang, W.; Zhang, Y. Y.; Qi, D. P.; Pan, S. W.; Loh, X. J.; Chen, X. D. Editable supercapacitors with customizable stretchability based on mechanically strengthened ultralong MnO2 nanowire composite. *Adv. Mater.* **2018**, *30*, 1704531.

(12) Zheng, S. S.; Xue, H. G.; Pang, H. Supercapacitors based on metal coordination materials. *Coord. Chem. Rev.* **2017**, 10.1016/j.ccr.2017.07.002.

(13) Li, Y. J.; Wang, G. L.; Wei, T.; Fan, Z. J.; Yan, P. Nitrogen and sulfur co-doped porous carbon nanosheets derived from willow catkin for supercapacitors. *Nano Energy* **2016**, *19*, 165−175.

(14) Zhu, Y. W.; Murali, S.; Stoller, M. D.; Ganesh, K. J.; Cai, W. W.; Ferreira, P. J.; Pirkle, A.; Wallace, R. M.; Cychosz, K. A.; Thommes, M.; Su, D.; Stach, E. A.; Ruoff, R. S. Carbon-based supercapacitors produced by activation of graphene. *Science* **2011**, *332*, 1537−1541.

(15) Stoller, M. D.; Park, S.; Zhu, Y. W.; An, J.; Ruoff, R. S. Graphene-based ultracapacitors. *Nano Lett.* **2008**, *8*, 3498−3502.

(16) Lai, F. L.; Miao, Y. E.; Zuo, L. Z.; Lu, H. Y.; Huang, Y. P.; Liu, T. X. Biomass-derived nitrogen-doped carbon nanofiber network: A facile template for decoration of ultrathin nickel-cobalt layered double hydroxide nanosheets as high-performance asymmetric supercapacitor electrode. *Small* **2016**, *12*, 3235−3244.

(17) Zhai, Y. P.; Dou, Y. Q.; Zhao, D. Y.; Fulvio, P. F.; Mayes, R. T.; Dai, S. Carbon materials for chemical capacitive energy storage. *Adv. Mater.* **2011**, *23*, 4828−4850.

(18) Deng, S.; Qi, X. D.; Zhu, Y. L.; Zhou, H. J.; Chen, F.; Fu, Q. A facile way to large-scale production of few-layered graphene via planetary ball mill. *Chin. J. Polym. Sci.* **2016**, *34*, 1270−1280.

(19) Yang, X. W.; Cheng, C.; Wang, Y. F.; Qiu, L.; Li, D. Liquid-mediated dense integration of graphene materials for compact capacitive energy storage. *Science* **2013**, *341*, 534−537.

(20) Stankovich, S.; Dikin, D. A.; Piner, R. D.; Kohlhaas, K. A.; Kleinhammes, A.; Jia, Y. Y.; Wu, Y.; Nguyen, S. Y.; Ruoff, R. S. Synthesis of graphene-based nanosheets via chemical reduction of exfoliated graphite oxide. *Carbon* **2007**, *45*, 1558−1565.

(21) Quintana, M.; Grzelczak, M.; Spyrou, K.; Kooi, B.; Bals, S.; Van Tendeloo, G.; Rudolf, P.; Prato, M. Production of large graphene sheets by exfoliation of graphite under high power ultrasound in the presence of tiopronin. *Chem. Commun.* **2012**, *48*, 12159−12161.

(22) Reina, A.; Jia, X. T.; Ho, J.; Nezich, D.; Son, H.; Bulovic, V.; Dresselhaus, M. S.; Kong, J. Large area, few-layer graphene films on arbitrary substrates by chemical vapor deposition. *Nano Lett.* **2009**, *9*, 30−35.

(23) Subramanya, B.; Bhat, D. K. Novel one-pot green synthesis of graphene in aqueous medium under microwave irradiation using a regenerative catalyst and the study of its electrochemical properties. *New J. Chem.* **2015**, *39*, 420−430.

(24) Lai, F. L.; Miao, Y. E.; Zuo, L. Z.; Zhang, Y. F.; Liu, T. X. Carbon aerogels derived from bacterial cellulose/polyimide composites as versatile adsorbents and supercapacitor electrodes. *ChemNanoMat* **2016**, *2*, 212−219.

(25) Hao, P.; Zhao, Z. H.; Tian, J.; Li, H. D.; Sang, Y. H.; Yu, G. W.; Cai, H. Q.; Liu, H.; Wong, C. P.; Umar, A. Hierarchical porous carbon aerogel derived from bagasse for high performance supercapacitor electrode. *Nanoscale* **2014**, *6*, 12120−12129.

(26) Sun, L.; Tian, C. G.; Li, M. T.; Meng, X. Y.; Wang, L.; Wang, R. H.; Yin, J.; Fu, H. G. From coconut shell to porous graphene-like nanosheets for high-power supercapacitors. *J. Mater. Chem. A* **2013**, *1*, 6462−6470.

(27) Tang, Y. X.; Deng, J. Y.; Li, W. L.; Malyi, O. I.; Zhang, Y. Y.; Zhou, X. R.; Pan, S. W.; Wer, J. Q.; Cai, Y. R.; Chen, Z.; Chen, X. D. Water-soluble sericin protein enabling stable solid-electrolyte inter-

phase for fast charging high voltage battery electrode. *Adv. Mater.* **2017**, *29*, 1701828.

(28) Li, X. R.; Ding, S. Y.; Xiao, X.; Shao, J. Y.; Wei, J. L.; Pang, H.; Yu, Y. N, S co-doped 3D mesoporous carbon-Co3Si2O5(OH)4 architectures for high-performance flexible pseudo-solid-state supercapacitors. *J. Mater. Chem. A* **2017**, *5*, 12774−12781.

(29) Pandolfo, A. G.; Hollenkamp, A. F. Carbon properties and their role in supercapacitors. *J. Power Sources* **2006**, *157*, 11−27.

(30) Ekimov, E. A.; Sidorov, V. A.; Bauer, E. D.; Mel'Nik, N. N.; Curro, N. J.; Thompson, J. D.; Stishov, S. M. Superconductivity in diamond. *Nature* **2004**, *428*, 542−545.

(31) Sun, X. J.; Zhang, Y. W.; Song, P.; Pan, J.; Zhuang, L.; Xu, W. L.; Xing, W. Fluorine-doped carbon blacks: Highly efficient metal-free electrocatalysts for oxygen reduction reaction. *ACS Catal.* **2013**, *3*, 1726−1729.

(32) Lai, F. L.; Huang, Y. P.; Zuo, L. Z.; Gu, H. H.; Miao, Y. E.; Liu, T. X. Electrospun nanofiber-supported carbon aerogel as a versatile platform toward asymmetric supercapacitors. *J. Mater. Chem. A* **2016**, *4*, 15861−15869.

(33) Zhang, Y. J.; Mori, T.; Ye, J. H.; Antonietti, M. Phosphorus-doped carbon nitride solid: Enhanced electrical conductivity and photocurrent generation. *J. Am. Chem. Soc.* **2010**, *132*, 6294−6295.

(34) Yu, X.; Park, H. S. Sulfur-incorporated, porous graphene films for high performance flexible electrochemical capacitors. *Carbon* **2014**, *77*, 59−65.

(35) Lee, W. J.; Maiti, U. N.; Lee, J. M.; Lim, J.; Han, T. H.; Kim, S. O. Nitrogen-doped carbon nanotubes and graphene composite structures for energy and catalytic applications. *Chem. Commun.* **2014**, *50*, 6818−6830.

(36) Yang, Z.; Yao, Z.; Li, G. F.; Fang, G. Y.; Nie, H. G.; Liu, Z.; Zhou, X. M.; Chen, X. A.; Huang, S. M. Sulfur-doped graphene as an efficient metal-free cathode catalyst for oxygen reduction. *ACS Nano* **2012**, *6*, 205−211.

(37) Zhou, G. M.; Zhao, Y. B.; Manthiram, A. Dual-confined flexible sulfur cathodes encapsulated in nitrogen-doped double-shelled hollow carbon spheres and wrapped with graphene for Li-S batteries. *Adv. Energy Mater.* **2015**, *5*, 1402263.

(38) Hou, H. Q.; Ge, J. J.; Zeng, J.; Li, Q.; Reneker, D. H.; Greiner, A.; Cheng, S. Z. D. Electrospun polyacrylonitrile nanofibers containing a high concentration of well-aligned multiwall carbon nanotubes. *Chem. Mater.* **2005**, *17*, 967−973.

(39) Gao, F.; Qu, J. Y.; Zhao, Z. B.; Wang, Z. Y.; Qiu, J. S. Nitrogen-doped activated carbon derived from prawn shells for high-performance supercapacitors. *Electrochim. Acta* **2016**, *190*, 1134−1141.

(40) Zhao, Y. Q.; Lu, M.; Tao, P. Y.; Zhang, Y. J.; Gong, X. T.; Yang, Z.; Zhang, G. Q.; Li, H. L. Hierarchically porous and heteroatom doped carbon derived from tobacco rods for supercapacitors. *J. Power Sources* **2016**, *307*, 391−400.

(41) Buckel, F.; Effenberger, F.; Yan, C.; Golzhauser, A.; Grunze, M. Influence of aromatic groups incorporated in long-chain alkanethiol self-assembled monolayers on gold. *Adv. Mater.* **2000**, *12*, 901−905.

(42) Gu, W. T.; Sevilla, M.; Magasinski, A.; Fuertes, A. B.; Yushin, G. Sulfur-containing activated carbons with greatly reduced content of bottle neck pores for double-layer capacitors: A case study for pseudocapacitance detection. *Energy Environ. Sci.* **2013**, *6*, 2465−2476.

(43) Long, C. L.; Qi, D. P.; Wei, T.; Yan, J.; Jiang, L. L.; Fan, Z. J. Nitrogen-doped carbon networks for high energy density supercapacitors derived from polyaniline coated bacterial cellulose. *Adv. Funct. Mater.* **2014**, *24*, 3953−3961.

(44) Wang, Q.; Yan, J.; Wei, T.; Feng, J.; Ren, Y. M.; Fan, Z. J.; Zhang, M. L.; Jing, X. Y. Two-dimensional mesoporous carbon sheet-like framework material for high-rate supercapacitors. *Carbon* **2013**, *60*, 481−487.

(45) Ling, Z.; Wang, Z. Y.; Zhang, M. D.; Yu, C.; Wang, G.; Dong, Y. F.; Liu, S. H.; Wang, Y. W.; Qiu, J. S. Sustainable synthesis and assembly of biomass-derived B/N co-doped carbon nanosheets with ultrahigh aspect ratio for high-performance supercapacitors. *Adv. Funct. Mater.* **2016**, *26*, 111−119.

(46) Raymundo-Pinero, E.; Leroux, F.; Beguin, F. A high-performance carbon for supercapacitors obtained by carbonization of a seaweed biopolymer. *Adv. Mater.* **2006**, *18*, 1877−1882.

(47) Bello, A.; Manyala, N.; Barzegar, F.; Khaleed, A. A.; Momodu, D. Y.; Dangbegnon, J. K. Renewable pine cone biomass derived carbon materials for supercapacitor application. *RSC Adv.* **2016**, *6*, 1800−1809.

(48) Lei, Z.; Christov, N.; Li, L. Z.; Zhao, X. S. Mesoporous carbon nanospheres with an excellent electrocapacitive performance. *J. Mater. Chem.* **2011**, *21*, 2274−2281.

(49) Chen, Y. M.; Li, X. Y.; Park, K.; Song, J.; Hong, J. H.; Zhou, L. M.; Mai, Y. W.; Huang, H. T.; Goodenough, J. B. Hollow carbon-nanotube/carbon-nanofiber hybrid anodes for Li-ion batteries. *J. Am. Chem. Soc.* **2013**, *135*, 16280−16283.

(50) Cheng, Q.; Tang, J.; Ma, J.; Zhang, H.; Shinya, N.; Qin, L. C. Graphene and carbon nanotube composite electrodes for supercapacitors with ultra-high energy density. *Phys. Chem. Chem. Phys.* **2011**, *13*, 17615−17624.

(51) Jeon, I.; Ju, M. J.; Xu, J. T.; Kim, M. J.; Choi, I. T.; Kim, H. M.; Kim, J. C.; Lee, J. J.; Liu, H. K.; Kim, H. K.; Dou, S. X.; Dai, L. M.; Baek, J. B. Edge-fluorinated graphene nanoplatelets as high performance electrodes for dye-sensitized solar cells and lithium ion batteries. *Adv. Funct. Mater.* **2015**, *25*, 1170−1179.

(52) Wang, C. Y.; Li, D.; Too, C. O.; Wallace, G. G. Electrochemical properties of graphene paper electrodes used in lithium batteries. *Chem. Mater.* **2009**, *21*, 2604−2606.

(53) Kresse, G.; Hafner, J. Ab initio molecular dynamics for liquid metals. *Phys. Rev. B: Condens. Matter Mater. Phys.* **1993**, *47*, 558−561.

(54) Blöchl, P. E. Projector augmented-wave method. *Phys. Rev. B: Condens. Matter Mater. Phys.* **1994**, *50*, 17953−17979.

(55) Kresse, G.; Furthmüller, J. Efficient iterative schemes for ab initio total-energy calculations using a plane-wave basis set. *Phys. Rev. B: Condens. Matter Mater. Phys.* **1996**, *54*, 11169−11186.

(56) Kresse, G.; Joubert, D. From ultrasoft pseudopotentials to the projector augmented-wave method. *Phys. Rev. B: Condens. Matter Mater. Phys.* **1999**, *59*, 1758−1775.

(57) Perdew, J. P.; Burke, K.; Ernzerhof, M. Generalized gradient approximation made simple. *Phys. Rev. Lett.* **1996**, *77*, 3865−3868.

(58) Monkhorst, H. J.; Pack, J. D. Special points for Brillouin-zone integrations. *Phys. Rev. B* **1976**, *13*, 5188−5192.

(59) Park, S.; Vosguerichian, M.; Bao, Z. A review of fabrication and applications of carbon nanotube film-based flexible electronics. *Nanoscale* **2013**, *5*, 1727−1752.